

Solid-Solid Phononic Crystal with Strongly Time-Modulated Elastic Constituents

Matthew Li*,¹ Dmitrii Shymkiv*,^{1, a)} Ying Wu,² and Arkadii Krokhin^{1, b)}

¹⁾*Department of Physics, University of North Texas, Denton, Texas 76203, USA*

²⁾*Computer, Electrical, and Mathematical Science and Engineering (CEMSE) Division, King Abdullah University of Science and Technology (KAUST), Thuwal 23955-6900, Saudi Arabia*

(Dated: 15 October 2024)

A spatially periodic structure of heterogeneous elastic rods that periodically oscillate along their axes is proposed as a time-modulated 2D phononic crystal. Each rod is a bimetallic cylinder consisting of slices with significantly different elastic properties. The rods are imbedded in a solid matrix. Using plane wave expansion, it is shown that the dispersion equation is obtained from the solutions of a quadratic eigenvalue problem over the eigenfrequency ω . The coefficients of the corresponding quadratic polynomial are represented by infinite matrices defined in the space spanned by the reciprocal lattice vectors with elements depending on the mechanical oscillation frequency of the rods and Bloch vector \mathbf{k} . The calculated band structure exhibits both ω and \mathbf{k} band gaps. Due to the high elastic contrast between the materials in the bimetallic rods, a substantial depth of modulation is achieved, leading to a large gap to midgap ratio for the frequency, momentum and mixed band gaps.

^{a)}*These authors contributed equally.

^{b)}arkadii.krokhin@unt.edu

¹³ **I. INTRODUCTION**

¹⁴ Phononic crystals – periodically arranged acoustic inclusions in elastic medium¹ – are
¹⁵ designed to control the propagation of mechanical waves via the creation of frequency
¹⁶ band gaps^{2–5}, where wave propagation is forbidden. Since their emergence two decades
¹⁷ ago, phononic crystals have been applied in various engineering fields, including sound
¹⁸ insulation^{6,7}, vibration control, and waveguiding. The formation of frequency band gaps
¹⁹ is attributed to local resonances⁸ or Bragg scattering⁹, which result from the spatial modu-
²⁰ lation of the material parameters and time-harmonic behavior of the eigenmodes. Recently,
²¹ the temporal modulation of materials has attracted much attention¹⁰. From a fundamental
²² perspective, the time variable shares a similar role as the spatial variable in wave equa-
²³ tion: both appear in second order derivatives and exhibit periodic sinusoidal patterns in a
²⁴ homogeneous, stationary medium. Indeed, time brings a new degree of freedom to wave
²⁵ dynamics in modern metamaterials, enabling the manipulation of waves in a 4D space-time
²⁶ continuum^{14,15}. Nevertheless, the symmetry between coordinate and time variables is broken
²⁷ by the causality principle which, for example, does not allow wave propagation back in time.

²⁸ A time-modulated phononic crystal is a time-variant system where energy is not con-
²⁹ served. Introducing temporal modulation in addition to spatial modulation leads to
³⁰ the observation of many intriguing wave phenomena, such as time reversal,^{12,37} Fresnel
³¹ drag,¹⁶ signal amplification,^{17,18} nonreciprocal^{19–25} and unidirectional^{26–28} propagation, in-
³² verse prisms²⁹, and frequency conversion,³⁰ to name a few. For some interval of frequencies
³³ the energy of a sound wave can be extracted from the vibrating medium to compensate

34 dissipative losses¹⁸. These frequencies correspond to momentum gaps or mixed gaps in the
35 spectrum, which are regions where the eigenfrequency ω acquires a non-zero imaginary part.
36 Frequency gaps in the spectrum of a stationary phononic crystal occur if there is sufficiently
37 strong acoustic contrast between the scatterers and the background medium. Similarly, for
38 momentum or mixed gaps to open, sufficiently fast and deep temporal modulation is re-
39 quired. However, achieving these conditions is rather difficult since the elastic properties of
40 liquid and solids are generally stable and resistant to external perturbations. One common
41 method of time-dependent perturbation involves applying an AC voltage to a piezoelectric
42 constituent of the phononic crystal^{31–35}. This method of temporal modulation allows for
43 high modulation speed but achieves a relatively weak depth of modulation. Approaches
44 which rely on the modulation of a magnetic field to affect the stiffness of elastic materials
45 offer similar advantages and disadvantages^{36–38}. Purely mechanical methods of temporal
46 modulation are not well developed. Modulating the shape of the phononic crystal elements
47 typically requires the fabrication of elastic structures with complex shapes^{22,39}. A novel
48 method of mechanical modulation resulting in time-dependent boundary conditions and the
49 unidirectional pumping of acoustic energy was proposed in Ref. [40].

50 Here we propose a mechanically modulated 2D phononic crystal, where periodic time
51 dependence is introduced through the oscillatory motion of bimaterial rods along their axes
52 of symmetry. This method of mechanical modulation preserves the shape of the unit cell
53 and the scatterers, while causing the elastic properties of the scatterers to become time-
54 dependent. We specifically consider bimetallic aluminum-copper rods, which provide a large
55 modulation depth due to the high elastic contrast between the materials. As a result, the

56 momentum and mixed gaps occur at relatively low modulation frequencies. Using the plane-
57 wave expansion method, the wave equation is reduced to a quadratic eigenvalue problem
58 where the eigenvalues define the dispersion of sound waves $\omega = \omega(k)$ within the crystal. The
59 analytical properties of the dispersion relation within the mixed gaps are analyzed in the
60 complex planes of ω and k .

61 **II. SYSTEM GEOMETRY**

62 We consider the propagation of sound in a two-dimensional spatiotemporal phononic
63 crystal, where elastic parameters vary periodically in both space and time. The scatterers
64 are bi-material rods distributed in a square lattice that all vertically oscillate in phase with
65 frequency f_{vib} , see Fig. 1. For our study, the scatterer radius and unit cell period were set to
66 $R = 6$ cm and $a = 15$ cm respectively, leading to a filling fraction of cylinders $f \approx 0.5$. When
67 we study solid constituents, the scatterers are bimetallic (Cu-Al) rods and the background
68 matrix is epoxy. For the time modulation to essentially affect propagation of sound, the
69 frequency of modulation must be comparable to the frequency of sound. Thinking towards
70 experimental feasibility, the vibration frequencies necessary for deep temporal modulation
71 can be achieved by manipulating gear ratios or by having multiple material slices pass
72 through the plane of observation per rod oscillation.

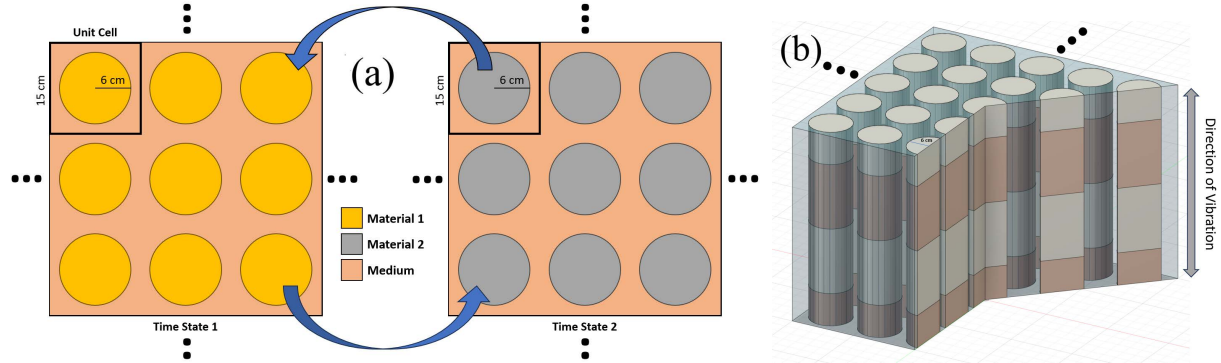


FIG. 1. Geometrical scheme for experimentally feasible spatiotemporal 2D phononic crystal consisting of oscillating bi-material rods arranged in a square lattice imbedded in elastic background.

a) On the top view the scatterer material periodically swaps between two types. b) Bimetallic rods oscillate in phase vertically, periodically switching the material of the scatterers for sound wave propagating in the horizontal direction.

⁷⁴ III. THE EIGENVALUE PROBLEM FOR SPATIOTEMPORAL PHONONIC
⁷⁵ CRYSTALS

⁷⁶ In inhomogeneous elastic media, where the mechanical properties may also depend on
⁷⁷ time, the wave equation for the displacement vector $\mathbf{u}(\mathbf{r}, t)$ in an elastic wave can be written
⁷⁸ in the following form³⁻⁵:

$$\frac{\partial}{\partial t} \left(\rho \frac{\partial}{\partial t} u_i \right) = \nabla \cdot (\mu \nabla u_i) + \nabla \cdot \left(\mu \frac{\partial \mathbf{u}}{\partial x_i} \right) + \frac{\partial}{\partial x_i} [(\lambda - 2\mu) \nabla \cdot \mathbf{u}], \quad i = x, y, z. \quad (1)$$

⁷⁹ Here, $\rho(\mathbf{r}, t)$ is the mass density and $\lambda(\mathbf{r}, t)$ and $\mu(\mathbf{r}, t)$ are the Lamé parameters. In a
⁸⁰ spatiotemporal phononic crystal the periodic functions $\rho(\mathbf{r}, t)$, $\lambda(\mathbf{r}, t)$, and $\mu(\mathbf{r}, t)$ in Eq. (1)

⁸¹ can be expanded over plane waves:

$$\rho(\mathbf{r}, t) = \sum_{\mathbf{G}} \sum_{\Omega} \rho(\mathbf{G}, \Omega) e^{i(\mathbf{G} \cdot \mathbf{r} - \Omega t)}, \quad (2)$$

$$\lambda(\mathbf{r}, t) = \sum_{\mathbf{G}} \sum_{\Omega} \lambda(\mathbf{G}, \Omega) e^{i(\mathbf{G} \cdot \mathbf{r} - \Omega t)}, \quad (3)$$

$$\mu(\mathbf{r}, t) = \sum_{\mathbf{G}} \sum_{\Omega} \mu(\mathbf{G}, \Omega) e^{i(\mathbf{G} \cdot \mathbf{r} - \Omega t)}, \quad (4)$$

⁸² where \mathbf{G} are the reciprocal lattice vectors and $\Omega = 2\pi n f_{vib}$ for $n = 0, \pm 1, \pm 2, \dots$. The

⁸³ explicit definition of $\rho(\mathbf{r}, t)$ is

$$\rho(\mathbf{r}, t) = \rho_a(t)\theta(\mathbf{r}) + \rho_b(1 - \theta(\mathbf{r})), \quad (5)$$

$$\rho_a(t) = \rho_1\Theta(t) + \rho_2(1 - \Theta(t)), \quad (6)$$

⁸⁴ where two Heaviside step functions are introduced

$$\theta(\mathbf{r}) = \begin{cases} 1 & \text{if } \mathbf{r} \subset \text{scatterer} \\ 0 & \text{otherwise} \end{cases}, \quad (7)$$

$$\Theta(t) = \begin{cases} 1 & \text{if } t \in [-T/4, T/4] \\ 0 & \text{if } t \in (-T/2, T/4) \cup [T/4, T/2] \end{cases}. \quad (8)$$

⁸⁵ Both $\lambda(\mathbf{r}, t)$ and $\mu(\mathbf{r}, t)$ are defined in a similar manner. The Fourier component $\rho(\mathbf{G}, \Omega)$

⁸⁶ can be calculated using Eqs. (5) and (6) to be

$$\rho(\mathbf{G}, \Omega) = \begin{cases} \frac{1}{2}(\rho_1 + \rho_2)f + \rho_b(1 - f) & \text{if } \mathbf{G} = 0, \Omega = 0 \\ 2f \frac{J_1(GR)}{GR} \left[\frac{1}{2}(\rho_1 + \rho_2) - \rho_b \right] & \text{if } \mathbf{G} \neq 0, \Omega = 0 \\ f(\rho_1 - \rho_2) \frac{\sin(\pi n/2)}{\pi n} & \text{if } \mathbf{G} = 0, \Omega \neq 0 \\ 2f(\rho_1 - \rho_2) \frac{J_1(GR)}{GR} \frac{\sin(\pi n/2)}{\pi n} & \text{if } \mathbf{G} \neq 0, \Omega \neq 0 \end{cases}. \quad (9)$$

87 Here, $f = \pi R^2/a^2$ is the filling fraction of the cylinders, n is the integer defining the order
 88 of the temporal Fourier component in the relation $\Omega = 2\pi n f_{vib}$, and $J_1(x)$ is the Bessel
 89 function of the first kind. Material parameters of the constituents of the rods are marked
 90 by subindexes 1 and 2 and the background material is marked by subindex b . Formulas for
 91 the Fourier coefficients of λ and μ have similar form. Oftentimes, in theoretical studies, the
 92 dependence of the material parameters (dielectric function, elastic parameters, etc) on t and
 93 \mathbf{r} are presented in a separable form, i.e., as the product of a time-dependent function and
 94 a coordinate-dependent function⁴³. This strongly simplifies solution of the corresponding
 95 wave equation. We consider the more general case of a non-separable spatiotemporal depen-
 96 dence as indicated in Eqs. (5) and (6). Although the Fourier components of the material
 97 parameters turn out to be separable in Eq. (9), this does not lead to any simplification of
 98 the wave equation in Fourier representation.

99 After expanding the displacement vector $\mathbf{u}(\mathbf{r}, t)$ in Eq. (1) over plane waves and applying
 100 Bloch/Floquet theorem,

$$\mathbf{u}(\mathbf{r}, t) = e^{i(\mathbf{k} \cdot \mathbf{r} - \omega t)} \sum_{\mathbf{G}} \sum_{\Omega} \mathbf{u}(\mathbf{G}, \Omega) e^{i(\mathbf{G} \cdot \mathbf{r} - \Omega t)}, \quad (10)$$

101 the following infinite set of linear homogeneous equations were obtained for the vector Fourier
 102 components $\mathbf{u}(\mathbf{G}, \Omega) = (u_x(\mathbf{G}, \Omega), u_y(\mathbf{G}, \Omega), u_z(\mathbf{G}, \Omega))$:

$$\begin{aligned}
 & \sum_{\mathbf{G}'} \sum_{\Omega'} \rho(\mathbf{G} - \mathbf{G}', \Omega - \Omega') (\Omega' + \omega) (\Omega + \omega) \mathbf{u}(\mathbf{G}', \Omega') = \\
 & \sum_{\mathbf{G}'} \sum_{\Omega'} (\mathbf{k} + \mathbf{G}') \cdot (\mathbf{k} + \mathbf{G}) \mu(\mathbf{G} - \mathbf{G}', \Omega - \Omega') \mathbf{u}(\mathbf{G}', \Omega') + \sum_{\mathbf{G}'} \sum_{\Omega'} (\mathbf{k} + \mathbf{G}') \mu(\mathbf{G} - \mathbf{G}', \Omega - \Omega') (\mathbf{k} + \mathbf{G}) \cdot \mathbf{u}(\mathbf{G}', \Omega') \\
 & + \sum_{\mathbf{G}'} \sum_{\Omega'} (\mathbf{k} + \mathbf{G}) (\lambda(\mathbf{G} - \mathbf{G}', \Omega - \Omega') - 2\mu(\mathbf{G} - \mathbf{G}', \Omega - \Omega')) (\mathbf{k} + \mathbf{G}') \cdot \mathbf{u}(\mathbf{G}', \Omega'). \quad (11)
 \end{aligned}$$

103 For the mode with transverse polarization $\mathbf{u} = (0, 0, u_z)$ the last two terms in Eq. (11) vanish
 104 and this mode is uncoupled from the mixed mode with in-plane polarization $\mathbf{u} = (u_x, u_y, 0)$.
 105 The left-hand side of this equation is ω -dependent, and the right-hand side is \mathbf{k} -dependent.
 106 Considering Eq. (11) as a quadratic eigenvalue problem over ω , we introduce three 2×2 block
 107 matrices \hat{Q}_{ij} , \hat{L}_{ij} , and \hat{K}_{ij} to represent the matrix coefficients of ω^2 , ω , and ω^0 respectively:

$$\sum_{\mathbf{G}'} \sum_{\Omega'} \left[\omega^2 \hat{Q}_{ij}(\mathbf{G} - \mathbf{G}', \Omega - \Omega') + \omega \hat{L}_{ij}(\mathbf{G}, \mathbf{G}', \Omega, \Omega') + \hat{K}_{ij}(\mathbf{k}, \mathbf{G}, \mathbf{G}', \Omega, \Omega') \right] u_j(\mathbf{G}', \Omega') = 0. \quad (12)$$

108 It is clear from Eq. (11) that $\hat{Q}_{ij}, \hat{L}_{ij} \propto \delta_{ij}$.

109 For every value of Bloch vector \mathbf{k} , the eigenvalue problem in Eq. (12) gives an infinite
 110 number of possible values of ω , which are the eigenfrequencies for the band structure of
 111 the crystal. Since the matrices \hat{Q}_{ij} , \hat{L}_{ij} , and \hat{K}_{ij} all depend explicitly on $\Omega = 2\pi n f_{vib}$, the
 112 band structure of the spatiotemporal phononic crystal depends essentially on the frequency
 113 of mechanical modulation.

114 The spectrum of eigenfrequencies ω for the quadratic eigenvalue problem can be calculated
 115 by the method of linearization⁴⁵ that reduces Eq. (12) to the following linear eigenvalue
 116 problem of twice larger rank:

$$\begin{bmatrix} \hat{\mathbf{O}} & \hat{\mathbf{I}} \\ -\hat{\mathbf{K}} & -\hat{\mathbf{L}} \end{bmatrix} \begin{bmatrix} \mathbf{u} \\ \omega \mathbf{u} \end{bmatrix} = \omega \begin{bmatrix} \hat{\mathbf{I}} & \hat{\mathbf{O}} \\ \hat{\mathbf{O}} & \hat{\mathbf{Q}} \end{bmatrix} \begin{bmatrix} \mathbf{u} \\ \omega \mathbf{u} \end{bmatrix}, \quad (13)$$

117 which has the same eigenvalues as Eq. (12). Here, $\hat{\mathbf{O}}$ and $\hat{\mathbf{I}}$ are respectively the zero and
 118 identity matrices, each having the same dimensionality over \mathbf{G} and Ω as matrices $\hat{\mathbf{Q}}, \hat{\mathbf{L}}$, and
 119 $\hat{\mathbf{K}}$.

120 Because the structure we consider enforces periodicity in both space and time, the eigen-
 121 values $\omega(\mathbf{k})$ calculated from Eq. (13) generate a band structure folded into the first temporal
 122 and spatial Brillouin zones. This produces a messy pattern where low-frequency bands over-
 123 lap with high-frequency bands. Due to a finite number of plane waves used in subsequent
 124 numerical calculations of the band structure, the low-frequency bands are calculated with
 125 much higher accuracy than the high-frequency bands. In the next sections, we demonstrate
 126 how to leave only the low-frequency bands, which are the most important for practical ap-
 127 plications, by unfolding the band structure. To illustrate the unfolding procedure, we first
 128 consider a spatiotemporal phononic crystal of fluids, where only pure longitudinal waves
 129 propagate, leaving less bands to study than in the case of solid constituents. Although the
 130 proposed method of mechanical modulation can hardly be realized for a phononic crystal of
 131 fluids, we still consider this structure to demonstrate the unfolding procedure in a simpler
 132 case.

133 **IV. BAND STRUCTURE CALCULATIONS. FLUID CONSTITUENTS**

134 The band structure of the spatiotemporal phononic crystal with the geometry depicted
 135 in Fig. 1 and elastic parameters listed in Table I is numerically calculated for discrete
 136 values of \mathbf{k} lying along ΓX direction. The background matrix is water, and the bi-material
 137 rods contain glycerin and acetone. We consider that these three fluid are inviscid. For this
 138 phononic crystal of fluids, all three shear moduli vanish: $\mu_1 = \mu_2 = \mu_b = 0$ and $\lambda = \rho c^2$.

140 To numerically calculate the band structure, sums in Eq. (11) are truncated to leave
 141 a finite number of plane waves over G_x, G_y , and Ω in the Fourier expansions. In this

TABLE I. Material parameters of the fluid phononic crystal

	Material 1	Material 2	Background
Material Name	Acetone	Glycerin	Water
Density, $\frac{kg}{m^3}$	784	1260	1000
Speed of Sound, $\frac{m}{s}$	1170	1920	1400

142 regard, 121 spatial and 9 temporal plane waves, or 1089 plane waves in total, were found
 143 to provide sufficient convergence for all presented band structures. For this number of
 144 plane waves, the generalized eigenvalue problem in Eq. (13) requires the diagonalization of
 145 4356×4356 matrices. Here, the factor of four between the number of rows and columns of
 146 each matrix and number of plane waves is due to the linearization procedure in Eq. (13) and
 147 the vector nature of the eigenvalue problem ($i, j = 1, 2$). To address the resulting challenges
 148 in execution time, we parallelized our code and utilized the Texas Advanced Computing
 149 Center's Lonestar 6 Supercomputer. At this point, available RAM proved to be the limiting
 150 factor that prevented the consideration of more plane waves. This in turn prevented the
 151 attainment of good convergence for higher frequency bands.

152 The folded band structure showing the first and second temporal Brillouin zones of eigen-
 153 frequencies obtained directly from the numerical calculations is presented in Fig. 2a. The
 154 shown bands are a result of both horizontal and vertical folding to the first Brillouin zone,
 155 where $|k_x| < \pi/a$ and $|\omega| < \pi f_{\text{vib}}$. To consider only horizontal folding (folding along k_x)
 156 into the irreducible spatial Brillouin zone, we reversed the process of vertical folding by
 157 using a clustering algorithm to identify and manipulate the converged bands. The result of

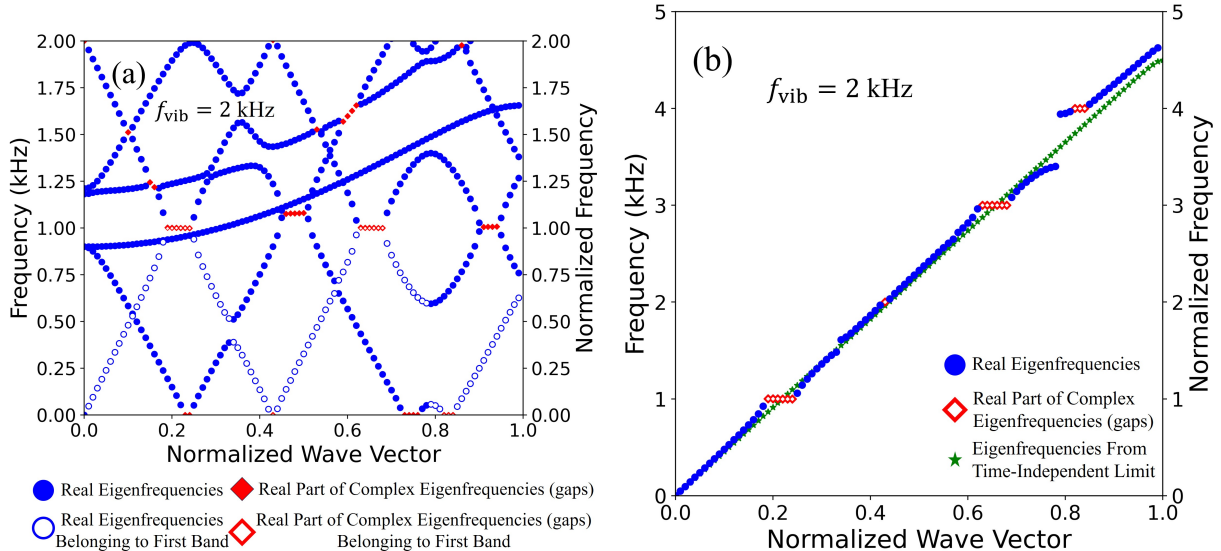


FIG. 2. (a) Folded band structure for ($f_{vib} = 2$ kHz). Two temporal Brillouin zones are shown.

Hollow dots indicate the states belonging to the lowest (acoustic) band. (b) Several temporal bands of the spatiotemporal crystal originated from the lowest band of the structure with $f_{vib} = 0$ (shown in green dots) are unfolded. Frequency and wave vector are normalized to the size of the corresponding Brillouin zone.

¹⁵⁸ this operation is Fig. 2b, where the band is exactly the hollow points from Fig. 2a. Also
¹⁵⁹ shown in Fig. 2b are green points corresponding to the first band of the system at the
¹⁶⁰ time-independent limit, $f_{vib} = 0$.

¹⁶¹ Although the unfolded band structure is much cleaner, it is only apparent from the
¹⁶² folded perspective that some gaps arise from the dispersed intersection of two folded bands.
¹⁶³ Here, we note that all nontrivial states lie inside the first Brillouin zone because modes
¹⁶⁴ with wavelength shorter than the spatial period do not represent a new physical state in a
¹⁶⁵ phononic crystal. As a result, the converged modes in Fig. 2a lying above the first temporal
¹⁶⁶ Brillouin zone repeat the vibrating states from the first zone. In other words, the unfolding

167 procedure does not add a new information to the dispersion of sound in a spatiotemporal
 168 phononic crystal. However, the unfolded picture does allow us to clearly see how temporal
 169 modulation has affected the dispersion of sound in relation to the time-independent limit
 170 of the crystal. In this respect, two frequency gaps near 1.5 and 3.5 kHz are opened. To
 171 contrast, frequency bandgaps do not appear within the lowest (acoustic) propagating band
 172 for stationary phononic crystals.

173 Additionally, the band structure in Fig. 2 exhibits momentum gaps – a feature attributed
 174 to spatiotemporal photonic and phononic crystals^{41–43}. It is well known that states within
 175 the frequency band gap have complex Bloch vector $\mathbf{k}(\omega) = \mathbf{k}'(\omega) + i\mathbf{k}''(\omega)$, which decay
 176 exponentially along the direction \mathbf{k}' and represent the evanescent modes in the spectrum.

177 In an analogous manner, the momentum band gap states have complex Floquet frequency
 178 $\omega(\mathbf{k}) = \omega' \pm i\omega''(\mathbf{k})$. This implies that, depending on the sign of the imaginary part, the
 179 sound wave amplitude may either decay or grow with time. This is achieved by either
 180 dumping energy to or absorbing energy from the time-dependent medium.

181 Some tuning in the frequency of modulation may lead to overlapping frequency and
 182 momentum gaps, forming a mixed momentum-frequency gap. The eigenstates within a
 183 mixed gap have complex ω and k . Depending on the values of ω'' and k'' , the amplitude of
 184 the eigenstates within a mixed bandgap may decay or grow exponentially⁴³. An example of
 185 eigenstates belonging to a mixed bandgap is studied in the next section.

	Material 1	Material 2	Background
Material Name	Aluminum	Copper	Epoxy
Density, $\frac{kg}{m^3}$	2700	8960	1200
Young's Modulus, GPa	70	110	4.35
Poisson Ratio	0.33	0.35	0.30

TABLE II. Elastic parameters for the materials of the spatiotemporal phononic crystal depicted in Fig. 1. Aluminum and copper are used as the two scatterer material, while epoxy permanently remains as the background material.

¹⁸⁶ **V. BAND STRUCTURE CALCULATIONS. SOLID CONSTITUENTS**

¹⁸⁷ The material parameters used in our numerical study of solid spatiotemporal phononic
¹⁸⁸ crystals are shown in Table II. Aluminum and copper were chosen as the two scatterer
¹⁸⁹ materials because of their high elastic contrast, offering deep temporal modulation. The use
¹⁹⁰ of epoxy as the background material further provided a high elastic contrast with each of
¹⁹¹ the metals.

¹⁹² Using the parameters in Table II, we present the band structure for the system in Fig. 1
¹⁹³ at vibrational frequencies of $f_{vib} = 2$ kHz and $f_{vib} = 4$ kHz in Figs. 3a and 3b respectively.
¹⁹⁴ For solid constituents, each band structure has two lowest propagation (acoustic) bands
¹⁹⁵ corresponding to elastic waves with transverse and mixed polarization. Our numerical cal-
¹⁹⁶ culations returned both purely real and complex eigenfrequencies, which are represented by
¹⁹⁷ the blue dots and red diamonds in Fig. 3 and correspond to propagation bands and gapped

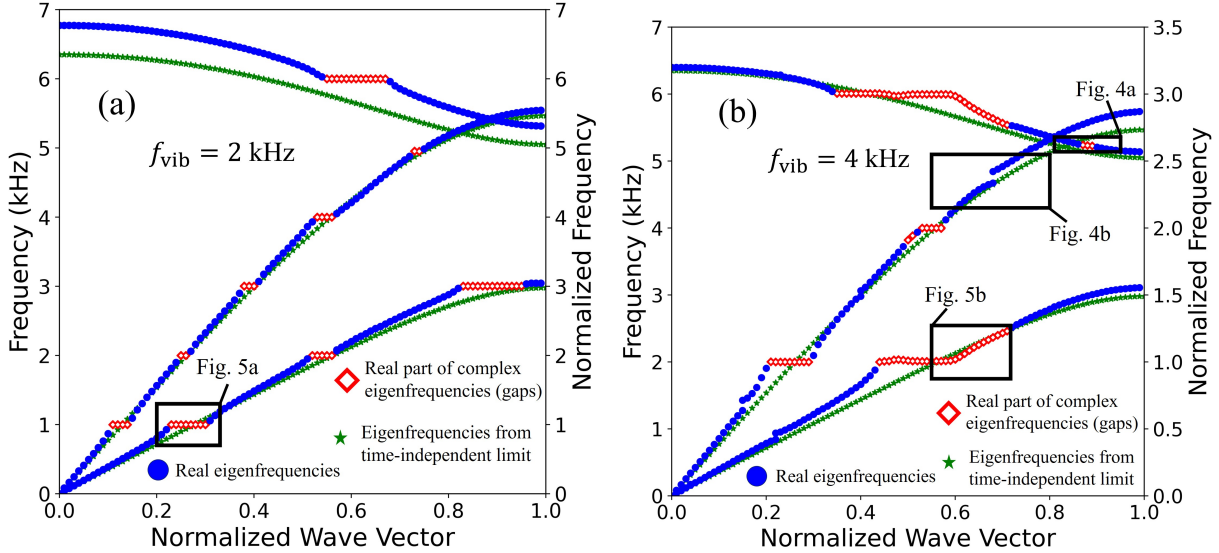


FIG. 3. Unfolded band structures for the system in Fig. 1 and material parameters in Table II

along the ΓX direction for two vibrational frequencies: (a) $f_{vib} = 2$ kHz and (b) $f_{vib} = 4$ kHz. The band structure for the time-independent crystal, where $f_{vib} = 0$, is shown in green dots.

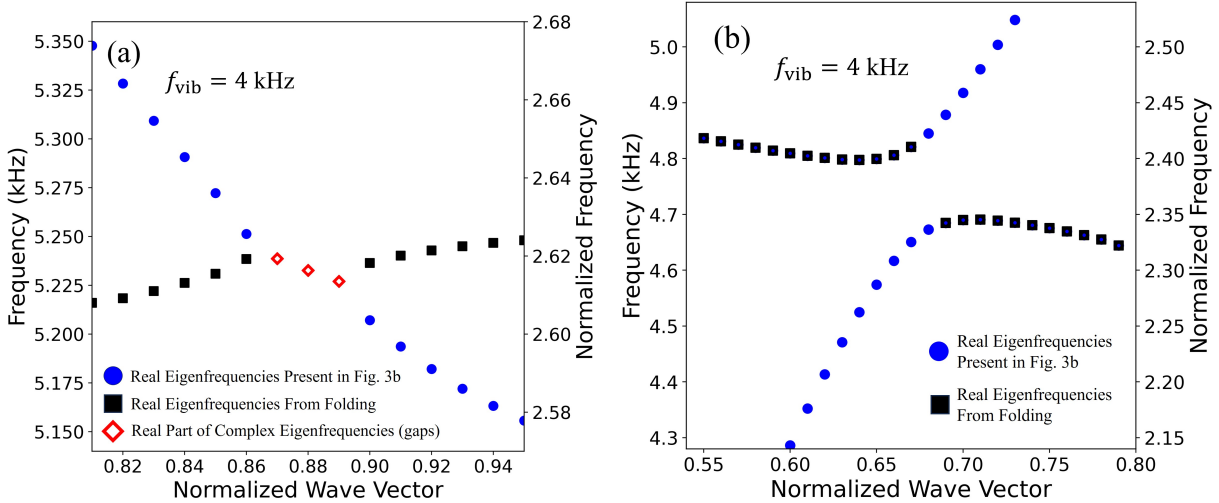


FIG. 4. Formation of band gaps inside the spatial Brillouin zone for $f_{vib} = 4$ kHz. The (a) mixed and (b) frequency gap appear due to avoid crossing of originally intersecting (degenerate) bands as a result of time-dependent perturbation.

¹⁹⁸ regions respectively. The eigenfrequencies with nonzero imaginary part are associated with
¹⁹⁹ momentum and mixed band gap states.

²⁰⁰ At the time-independent limit $f_{vib} \rightarrow 0$ (marked by green dots in Fig. 3), the calculation
²⁰¹ was found to correctly return a band structure identical to that of the time-independent
²⁰² binary elastic composite with scatterer parameters equal to the average of the metal pa-
²⁰³ rameters in Table II and background parameters remaining equivalent to those of epoxy.

²⁰⁴ For low modulation frequencies, momentum gaps were observed to appear at the edges of
²⁰⁵ the temporal Brillouin zones at Floquet frequencies $n\pi f_{vib}$ for an integer n . In the limit
²⁰⁶ $f_{vib} \rightarrow 0$, the system becomes time-independent and the momentum gaps disappear. As the
²⁰⁷ vibrational frequency increases, these momentum gaps at the edges of time Brillouin zones
²⁰⁸ smoothly increase in width.

²⁰⁹ For higher modulation frequencies, the momentum gaps begin to emerge away from the
²¹⁰ edges of the temporal and spatial Brillouin zones (see Fig. 3b). Since in a spatiotemporal
²¹¹ phononic crystal the bands repel in the $\omega - k$ plane (unlike repulsion along ω -axis for
²¹² stationary phononic crystals), these gaps may be frequency, momentum, or mixed gaps.

²¹³ Additionally, gaps formation can be due to lifting of degeneracy of two previously inter-
²¹⁴ secting bands (see Fig. 4). These gaps can be physically attributed to the fact that energy
²¹⁵ in the system is no longer conserved and the states are characterized by quasienergy⁴⁴. As
²¹⁶ a note, the bands composed of solid black squares in Fig. 4 do not belong to the first three
²¹⁷ bands, so they are not visible in Fig. 3b. Rather, the intersection appears when bands
²¹⁸ are folded down into the first temporal Brillouin zone by the mechanism discussed in the
²¹⁹ previous section, allowing the higher bands to interfere with the lower bands. For instance,

220 suppose the band structure of a stationary phononic crystal was artificially folded into the
221 first temporal Brillouin zone. The new intersections between various bands would be the
222 regions where time modulation induced lifting or degeneracy may occur if the system were
223 to become time-dependent.

224 For every k within a momentum gap, the corresponding eigenfrequencies ω are always
225 doubled to form complex conjugates. This is due to isotropy of the scatterers. If the scatter-
226 ers are centrally symmetric, as in our case, the Fourier coefficients of the elastic parameters
227 become real (see Eq. (9)), i.e., all the coefficients in the eigenvalue problems Eqs. (11)-(13)
228 are also real. This leads to real coefficients in the corresponding characteristic polynomials,
229 forcing the roots of these polynomials to be conjugate complex numbers. Therefore, the mo-
230 mentum gaps of a spatiotemporal phononic crystal with central-symmetric scatterers always
231 contain modes with amplitudes growing and decaying in time at the same rate. As a note,
232 this is not the case for a crystal where the scatterers do not possess central symmetry. In
233 this general case, the Fourier coefficients in the expansions Eqs. (2)-(4) are complex.

234 An example showing that all complex eigenfrequencies are conjugates in our case is pre-
235 sented in Fig. 5. In Fig. 5a particularly, a momentum gap near the edge of the first temporal
236 Brillouin zone of the crystal with $f_{vib} = 2$ kHz is shown. The curves shown are a result of
237 level repulsion. Instead of two bands linearly crossing near the edges of the temporal Bril-
238 louin zones, a periodic time-dependent perturbation lifts the degeneracy, replacing it with
239 the hyperbolic repulsion of bands. The eigenvalues inside the momentum gap are complex
240 with equal real parts and elliptic behavior of their imaginary parts,

$$\omega(k) = \omega_0 \pm ib\sqrt{1 - \frac{(k - k_0)^2}{a^2}}. \quad (14)$$

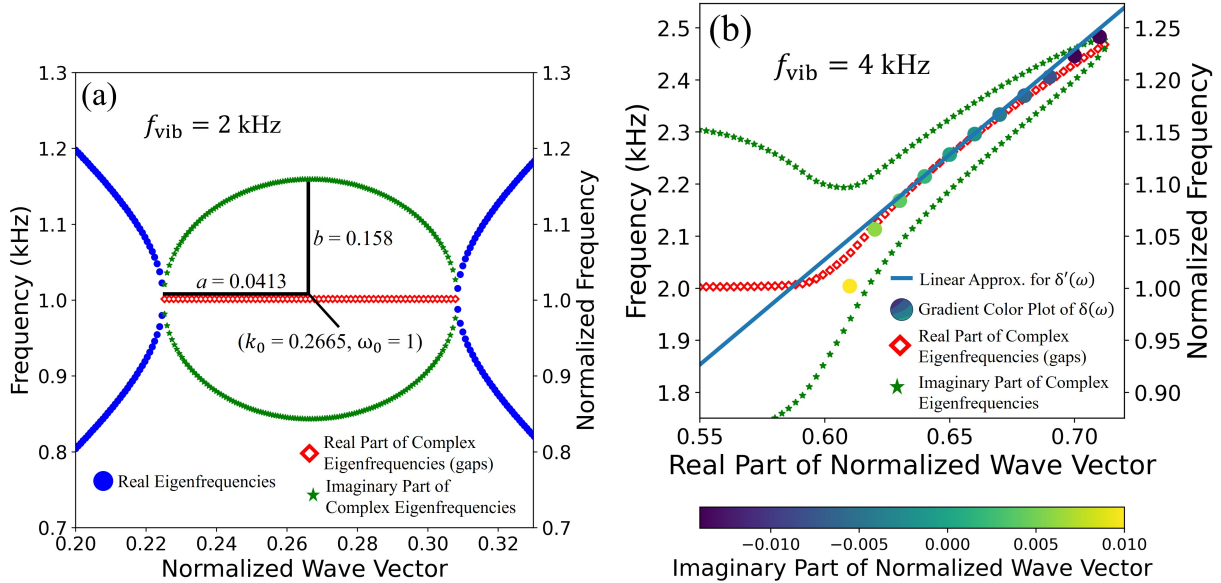


FIG. 5. (a) Hyperbolic lifting of two bands from the folded band structure leading to the formation of the lowest momentum gap in Fig. 3a. This gap appears at the edge of the first temporal Brillouin zone. Purely real eigenvalues are plotted in blue, and the real and imaginary parts of complex eigenvalues are plotted in red and green respectively. The value of the imaginary part is indicated by the distance of green points from the red line. Perturbation-induced interaction between two intersecting bands leads to their hyperbolic repulsion and elliptic behavior of the imaginary parts of the eigenfrequencies. (b) Mixed bandgap formed by overlapping momentum and frequency gaps. The red diamonds and green dots contain information about the real ($\omega_0(k)$) and imaginary part ($\Omega(k)$) of each eigenfrequency. The straight blue line is the dependence $\delta'(\Delta)$ calculated for $k = 0.65$ using the linear approximation in Eq. (16). In particular, $\Omega(k) = 0.34i$ along this line. The real part of the complex Bloch vectors calculated using Eq. (13) are plotted as multicolored dots, where the color represents the imaginary part (δ'') of each k .

²⁴¹ Here, $a = 0.0413$ ($a = 0.00865 \text{ cm}^{-1}$) and $b = 0.158$ ($b = 158 \text{ Hz}$) are the semiaxes and
²⁴² $k_0 = 0.27$ ($k_0 = 0.056 \text{ cm}^{-1}$) and $\omega_0 = 1$ ($\omega_0 = 1 \text{ kHz}$) are the coordinates of the center of
²⁴³ the ellipse in Fig. 5a.

²⁴⁴ A more complicated and interesting situation arises if momentum and frequency gaps
²⁴⁵ overlap, leading to the formation of a mixed bandgap as shown in Fig. 5b. Unlike frequency
²⁴⁶ or momentum bandgaps, which are represented by vertical and horizontal intervals where
²⁴⁷ \mathbf{k} and ω take complex values, mixed bandgaps occupy a finite region in the $\omega - k$ plane
²⁴⁸ where both coordinates are essentially complex. While a mixed bandgap does not appear at
²⁴⁹ a modulation frequency of 2 kHz, there are multiple mixed bandgaps found at $f_{vib} = 4 \text{ kHz}$
²⁵⁰ in Fig. 3b. For instance, Fig. 4a shows the region of a narrow mixed bandgap lying above
²⁵¹ normalized frequency 1. A wider mixed bandgap lying within the lowest propagating band is
²⁵² blown-up in Fig. 5b. The vertical coordinates of the red and green dots were obtained from
²⁵³ the eigenvalue problem Eq. (13) by scanning the Bloch vector within the gap. The vertical
²⁵⁴ coordinate of each red dot gives the real part of the calculated complex eigenfrequency
²⁵⁵ $\omega(k) = \omega_0(k) \pm i\Omega_0(k)$. The corresponding imaginary part, $\pm\Omega_0(k)$, is represented by
²⁵⁶ the vertical distance between each green and red dot for every Bloch vector k . Since the
²⁵⁷ eigenfrequencies appear in conjugate pairs, each red dot is equidistant from a matching pair
²⁵⁸ of green dots.

²⁵⁹ Any point within a mixed gap not lying on the line of red dots is characterized by
²⁶⁰ complex values of ω and k . Within these mixed gaps, the analytic continuation of the
²⁶¹ function $\omega_0(k) \pm i\Omega_0(k)$ from the real axis k to a complex k -domain is given by the implicit
²⁶² dependence $f(\omega, k) = 0$. In the plane-wave expansion method, the function $f(\omega, k)$ is the

characteristic polynomial of the eigenvalue problem in Eq. (13). However, the complex roots of this polynomial are difficult to obtain numerically because the large size of our matrices leads to a very high-order characteristic polynomial. Therefore, for the frequencies lying close to the line of red dots, the analytic continuation can be approximated using perturbation theory, if the complex function $\omega_0(k) + i\Omega_0(k)$ is known.

For the dispersion relation $f(\omega, k) = 0$, where both arguments may be complex, small corrections to the frequency (Δ) and wave vector (δ) are related,

$$\Delta = -\delta \frac{\partial f / \partial k}{\partial f / \partial \omega} = \delta \frac{d\omega}{dk}. \quad (15)$$

If the correction Δ is a real number and the unperturbed frequency is $\omega_0(k) \pm i\Omega_0(k)$ is defined for real k , the wave vector acquires a complex correction $\delta = \delta' + i\delta''$, where

$$\delta' = \Delta \frac{d\omega_0/dk}{(d\omega_0/dk)^2 + (d\Omega_0/dk)^2}, \quad \delta'' = \mp \Delta \frac{d\Omega_0/dk}{(d\omega_0/dk)^2 + (d\Omega_0/dk)^2}. \quad (16)$$

These equations confirm that the Bloch vector and Floquet frequency are both complex within a mixed bandgap.

The linear relation between δ' and Δ is shown in Fig. 5b by the straight blue line for a Bloch vector of value $k = 0.65$ and an unperturbed frequency $\omega = \omega_0(k = 0.65) \pm i\Omega_0(k = 0.65) = 1.13 \pm i0.34$. To get the complex values of k beyond this linear approximation the eigenvalue problem Eq. (13) was solved with respect to k for the values of $\omega = \omega' \pm i0.34$, where ω' takes discrete values above and below $\omega_0 = 1.13$ within the mixed band gap.

The result of these calculations is plotted by the larger, multicolored dots, where the color gradient represents the imaginary part of k . These colored dots give complete information about the complex dispersion relation for the bandgap eigenstates having real Bloch vector

²⁸² $k = 0.65$ and $\Omega_0 = \pm 0.34$. The procedure can be repeated for every value of the Bloch
²⁸³ vector within the mixed bandgap. Note that the linear approximation Eq. (16) is valid for
²⁸⁴ a wide range of frequencies within the mixed bandgap.

²⁸⁵ The eigenstates within a mixed bandgap may gain energy from the vibrating environment.
²⁸⁶ The amplitude of an eigenstate with $k = k' + ik''$ and $\omega = \omega' + i\omega''$ changes with time as
²⁸⁷ $\exp[(\omega'' - \frac{k''}{k'}\omega')t]$. The eigenstates belonging to the red line in Fig. 5b grow as $\exp(\Omega_0 t)$,
²⁸⁸ ($\Omega_0 > 0$) since they have purely real values of k . The time evolution of a light beam
²⁸⁹ entering a spatiotemporal photonic crystal with parameters corresponding to frequency,
²⁹⁰ momentum, and mixed bandgaps was studied in Ref. [43], where an exponential growth
²⁹¹ in the amplitude of light waves was numerically confirmed. Our proposed method for the
²⁹² numerical calculation of the dispersion relation within a mixed gap is an alternative to that
²⁹³ proposed in Ref. [43]. In their case, the variables x and t in the wave equation were separated,
²⁹⁴ allowing separation constant λ to be used in Ref. [43] for a graphical representation of the
²⁹⁵ complex dispersion relation.

²⁹⁶ The period of modulation $T = 1/f_{vib}$ used in our calculations is essentially larger than
²⁹⁷ the time $t = a/c$ that it takes for a sound wave to cross the unit cell, i.e., $a f_{vib}/c \ll 1$.
²⁹⁸ This means that the modulation is practically adiabatic with respect to sound wave passing
²⁹⁹ through the unit cell. In the adiabatic regime, the momentum gaps in the lowest acoustic
³⁰⁰ band appear only at the edges of the temporal Brillouin zones, see Fig. 3a. For higher
³⁰¹ modulation frequencies, the momentum gaps in Fig 3b also appear in the bulk of the Brillouin
³⁰² zone. Moreover, the momentum gaps in Fig. 3b at times overlap with the frequency gaps.
³⁰³ In these overlapping regions, the amplitude of the states decays exponentially with path

length and grows exponentially with time. Different regimes of propagation may be realized depending on the rate of time and distance variation⁴³. If the rate of temporal growth exceeds the rate of appropriately normalized distance decay, a band gap mode behaves like a ghost mode propagating in a waveguide with strong biaxial anisotropy⁴⁶.

Note that while the frequency of modulation is relatively low, momentum band gaps with widths ranging from $\sim 5 - 10\%$ of the total width of the Brillouin zone still appear.

VI. CONCLUSION

We propose an experimentally feasible scheme for the temporal modulation of elastic properties in a 2D phononic crystal using periodically arranged, vibrating bi-material rods. Materials possessing high elastic contrast with each other are selected to induce strong spatial and temporal modulation within a medium where sound waves propagate.

Using plane wave expansion over coordinates and time, the wave equation for elastic deformation is reduced to a quadratic eigenvalue problem. Its solution for the eigenfrequency $\omega(\mathbf{k})$ is obtained by introducing three auxiliary matrices serving as coefficients for ω^2 , ω , and ω^0 . With these results, the band structure is numerically calculated for a hypothetical phononic crystal of glycerin-acetone rods in water and a practical solid phononic crystal of copper-aluminum rods in epoxy. In the case of solid constituents, several momentum bandgaps are already present at the relatively low frequency of modulation $f_{vib} = 2$ kHz. When the modulation frequency is increased to $f_{vib} = 4$ kHz, momentum and frequency gaps also overlap to form mixed frequency-momentum bandgaps.

324 We finally propose a numerical procedure to approximate the analytic continuation for
325 the dispersion relation $\omega = \omega(k)$ in the mixed bandgap zones, where both ω and k become
326 complex. This procedure is valid for general functions representing the dependence of the
327 elastic parameters on time and coordinates. In particular, it remains valid for functions with
328 non-separable variables.

329 **VII. ACKNOWLEDGEMENTS**

330 This work is supported by an EFRI grant No. 1741677 from the National Science Foun-
331 dation and by the Air Force Office of Scientific Research under award number FA9550-23-
332 1-0630.

333 **VIII. AUTHOR DECLARATIONS**

334 **Conflict of Interest**

335 The authors have no conflicts to disclose.

336 **IX. DATA AVAILABILITY**

337 The data that support the findings of this study are available from the corresponding
338 author upon reasonable request.

339 **REFERENCES**

340 ¹*Acoustic Metamaterials and Phononic Crystals*, Edited by Pierre A. Deymier (Springer

³⁴¹ Berlin, Heridelberg, 2013).

³⁴² ²M. S. Kushwaha, P. Halevi, L. Dobrzynski, and B. Djafari-Rouhani, Acoustic band struc-
³⁴³ ture of periodic elastic composites, Phys. Rev. Lett. **71**, 2022 (1993).

³⁴⁴ ³M.M. Sigalas, and E.N. Economou, Elastic and acoustic wave band structure, J. Sound
³⁴⁵ Vib., **158** (2), 377–382, (1992).

³⁴⁶ ⁴M.S. Kushwaha, P. Halevi, G. Martínez, L. Dobrzynski, and B. Djafari-Rouhani, Theory of
³⁴⁷ acoustic band structure of periodic elastic composites, Phys. Rev. B **49**, 2313-2322 (1994).

³⁴⁸ ⁵Manvir S. Kushwaha, Classical band structure of periodic elastic composites, International
³⁴⁹ Journal of Modern Physics B, **10**, 977 (1996).

³⁵⁰ ⁶R. Martínez-Sala, J. Sancho, J.V. Sánchez, V. Gómez, J. Llinares, and F. Meseguer, Sound
³⁵¹ attenuation by sculpture, Nature, bf 378, 241 (1995).

³⁵² ⁷J. V. Sánchez-Pérez, D. Caballero, R. Márquez-Sala, C. Rubio, J. Sánchez-Dehesa, F.
³⁵³ Meseguer, J. Llinares, and F. Gálvez, Sound attenuation by a two-dimensional array of
³⁵⁴ rigid cylinders, Phys. Rev. Lett. **80**, 5325 (1998).

³⁵⁵ ⁸Zhengyou Liu, Xixiang Zhang, Yiwei Mao, Y. Y. Zhu, Zhiyu Yang, C. T. Chan, and Ping
³⁵⁶ Sheng, Locally resonant sonic materials, Science **289**, 1734-1736 (2002).

³⁵⁷ ⁹Mahmoud I. Hussein, Michael J. Leamy, and Massimo Ruzzene, Dynamics of phononic
³⁵⁸ materials and structures: historical origins, recent progress, and future outlook, ASME
³⁵⁹ Appl. Mech. Rev., **66** (4), 040802 (2014).

³⁶⁰ ¹⁰C. Caloz and Z.-L. Deck-Léger, Spacetime metamaterials, Part I and II, IEEE Trans.
³⁶¹ Antennas Propag. **68**, 1569 (2020); *ibid* **68**, 1583 (2020).

- ³⁶² ¹¹Eran Lustig, Ohad Segal, Soham Saha, Colton Fruhling, Vladimir M. Shalaev, Alexandra
³⁶³ Boltasseva, and Mordechai Segev, Photonic time-crystals - fundamental concepts, Optics
³⁶⁴ Express **31**, 9165-9170 (2023).
- ³⁶⁵ ¹²Vincent Bacot, Matthieu Labousse, Antonin Eddi, Mathias Fink, and Emmanuel Fort,
³⁶⁶ Time reversal and holography with spacetime transformations, Nat. Phys. **12**, 972–977
³⁶⁷ (2016).
- ³⁶⁸ ¹³Brian L. Kim, Christopher Chong, and Chiara Daraio, Temporal refraction in an acoustic
³⁶⁹ phononic lattice, Phys. Rev. Lett. **133**, 077201 (2024).
- ³⁷⁰ ¹⁴Nader Engheta, Four-dimensional optics using time-varying metamaterials, Science **379**,
³⁷¹ 1190 (2023).
- ³⁷² ¹⁵Victor Pacheco-Peña, Diego M. Solís, and Nader Engheta, Time-varying electromagnetic
³⁷³ media: opinion, Opt. Mater. Express **12**, 3829 (2022).
- ³⁷⁴ ¹⁶P. A. Huidobro, E. Galiffi, S. Guenneau, R. V. Craster, and J. Pendry, Fresnel drag in
³⁷⁵ space–time-modulated metamaterials, Proc. Natl. Acad. Sci. U. S. A. **116**, 24943 (2019).
- ³⁷⁶ ¹⁷T. Koutserimpas, A. Alù, and R. Fleury, Parametric amplification and bidirectional invis-
³⁷⁷ ibility in PT-symmetric time-Floquet systems, Phys. Rev. A **97**, 013839 (2018).
- ³⁷⁸ ¹⁸Daniel Torrent, William J. Parnell, and Andrew N. Norris, Loss compensation in time-
³⁷⁹ dependent elastic metamaterials, Phys. Rev. B **97**, 014105 (2018).
- ³⁸⁰ ¹⁹Hussein Nassar, Behrooz Yousefzadeh, Romain Fleury, Massimo Ruzzene, Andrea Alù,
³⁸¹ Chiara Daraio, Andrew N. Norris, Guoliang Huang, and Michael R. Haberman, Nonre-
³⁸² ciprocity in acoustic and elastic materials, Nat. Rev. Mater. **5**, 667–685 (2020).

- ³⁸³ ²⁰H. Nassar, H. Chen, A. N. Norris, and G. L. Huang, Quantization of band tilting in
³⁸⁴ modulated phononic crystals, Phys. Rev. B **97**, 014305 (2018).
- ³⁸⁵ ²¹Yifan Wang, Behrooz Yousefzadeh, Hui Chen, Hussein Nassar, Guoliang Huang, and
³⁸⁶ Chiara Daraio, Observation of nonreciprocal wave propagation in a dynamic phononic
³⁸⁷ lattice, Phys. Rev. Lett. **121**, 194301 (2018).
- ³⁸⁸ ²²Benjamin M. Goldsberry, Samuel P. Wallen, and Michael R. Haberman, Non-reciprocal
³⁸⁹ wave propagation in mechanically-modulated continuous elastic metamaterials, J. Acoust.
³⁹⁰ Soc. Am. **146**, 782–788 (2019).
- ³⁹¹ ²³C. Shen, X. Zhu, J. Li, and S.A. Cummer, Nonreciprocal acoustic transmission in space-
³⁹² time modulated coupled resonators, Phys. Rev. B **100**, 054302 (2019).
- ³⁹³ ²⁴X. Zhu, J. Li, C. Shen, X. Peng, A. Song, L. Li, and S.A. Cummer, Non-reciprocal acoustic
³⁹⁴ transmission via space-time modulated membranes Appl. Phys. Lett. **116**, 034101 (2020).
- ³⁹⁵ ²⁵Runcheng Cai, Yabin Jin, Yan Pennec, Bahram Djafari-Rouhani, Timon Rabczuk, Xi-
³⁹⁶ aoying Zhuang, Broadband non-reciprocal wave suppression and frequency conversion by
³⁹⁷ active metabeams, Mechanical Systems and Signal Processing, **220**, 111656 (2024).
- ³⁹⁸ ²⁶Romain Fleury, Alexander B. Khanikaev, and Andrea Alù, Floquet topological insulators
³⁹⁹ for sound, Nat. Commun. **7**, 11744 (2016).
- ⁴⁰⁰ ²⁷H. Nassar, X.C. Xu, A.N. Norris, G.L. Huang, Modulated phononic crystals: Non-
⁴⁰¹ reciprocal wave propagation and Willis materials, Journal of the Mechanics and Physics
⁴⁰² of Solids **101**, 10–29 (2017).

- 403 ²⁸Xianchen Xu, Qian Wu, Hui Chen, Hussein Nassar, Yangyang Chen, Andrew Norris,
404 Michael R. Haberman , and Guoliang Huang, Phys. Rev. Lett. **125**, 253901 (2020).
- 405 ²⁹A. Akbarzadeh, N. Chamanara, and C. Caloz, Inverse prism based on temporal discontinuity
406 and spatial dispersion, Opt. Lett. **43**, 3297–3300 (2018).
- 407 ³⁰Kanghee Lee, Jaehyeon Son, Jagang Park, Byungsoo Kang, Wonju Jeon, Fabian Rotermund,
408 and Bumki Min, Linear frequency conversion via sudden merging of meta-atoms in
409 time-variant metasurfaces, Nat. Photonics **12**, 765–773 (2018).
- 410 ³¹B.S. Beck, K.A. Cunefare, M. Ruzzene, and Manuel Collet, Experimental analysis of a
411 cantilever beam with a shunted piezoelectric periodic array, Journal of Intelligent Material
412 Systems and Structures, **22**, 1177-1187 (2011).
- 413 ³²C. Croënne, J. O. Vasseur, O. Bou Matar, M.-F. Ponge, P. A. Deymier, A.-C. Hladky-
414 Hennion, and B. Dubus, Brillouin scattering-like effect and non-reciprocal propagation
415 of elastic waves due to spatio-temporal modulation of electrical boundary conditions in
416 piezoelectric media, Appl. Phys. Lett. **110**, 061901 (2017).
- 417 ³³J. Marconi, E. Riva, M. Di Ronco, G. Cazzulani, F. Braghin, and M. Ruzzene, Experi-
418 mental observation of nonreciprocal band gaps in a space-time-modulated beam using a
419 shunted piezoelectric array, Phys. Rev. Applied **13**, 031001 (2020).
- 420 ³⁴Wu Qian, Qian Honghua, Chen Yangyang, Huang Guoliang, Dynamic phononic crystals
421 with spatially and temporally modulated circuit networks, Acta Mechanica Sinica **39**,
422 723007 (2023).

Solid-Solid Phononic Crystal with Strongly Time-Modulated Elastic Constituents

- ⁴²³ ³⁵S. Tessier Brothelande, C. Croënne, F. Allein, J. O. Vasseur, M. Amberg, F. Giraud, and
⁴²⁴ B. Dubus, Experimental evidence of nonreciprocal propagation in space-time modulated
⁴²⁵ piezoelectric phononic crystals, *Appl. Phys. Lett.* **123**, 201701 (2023).
- ⁴²⁶ ³⁶Yangyang Chen, Xiaopeng Li, Hussein Nassar, Andrew N. Norris, Chiara Daraio, and
⁴²⁷ Guoliang Huang, Nonreciprocal wave propagation in a continuum-based metamaterial with
⁴²⁸ space-time modulated resonators, *Phys. Rev. Applied* **11**, 064052 (2019).
- ⁴²⁹ ³⁷Brian L. Kim , Christopher Chong , and Chiara Daraio, Temporal refraction in an acoustic
⁴³⁰ phononic lattice, *Phys. Rev. Lett.* **133**, 077201 (2024).
- ⁴³¹ ³⁸Christopher Chong, Brian Kim, Evelyn Wallace, and Chiara Daraio, Modulation insta-
⁴³² bility and wavenumber bandgap breathers in a time layered phononic lattice, *Phys. Rev.*
⁴³³ *Research* **6**, 023045 (2024).
- ⁴³⁴ ³⁹D. Psiachos and M.M. Sigalas, Band-gap tuning in two-dimensional spatiotemporal
⁴³⁵ phononic crystals, *Phys. Rev. Applied* **15**, 014022 (2021).
- ⁴³⁶ ⁴⁰Xianchen Xu, Qian Wu, Hui Chen, Hussein Nassar, Yangyang Chen, Andrew Norris,
⁴³⁷ Michael R. Haberman, and Guoliang Huang, Physical observation of a robust acoustic
⁴³⁸ pumping in waveguides with dynamic boundary, *Phys. Rev. Lett.* **125**, 253901 (2020).
- ⁴³⁹ ⁴¹Fabio Biancalana, Andreas Amann, Alexander V. Uskov, and Eoin P. O'Reilly, Dynamics
⁴⁴⁰ of light propagation in spatiotemporal dielectric structures *Phys. Rev. E* **75**, 046607 (2007).
- ⁴⁴¹ ⁴²J. R. Reyes-Ayona and P. Halevi, Observation of genuine wave vector (k or β) gap in a
⁴⁴² dynamic transmission line and temporal photonic crystals, *Appl. Phys. Lett.* **107**, 074101
⁴⁴³ (2015).

- ⁴⁴⁴ ⁴³Yonatan Sharabi, Alex Dikopoltsev, Eran Lustig, Yaakov Lumer, and Mordechai Segev,
⁴⁴⁵ Spatiotemporal photonic crystals, Optica **9**, 585-592 (2022).
- ⁴⁴⁶ ⁴⁴Qian Wu, Hui Chen, Hussein Nassar, Guoliang Huang, Non-reciprocal Rayleigh wave
⁴⁴⁷ propagation in space-time modulated surface, Journal of the Mechanics and Physics of
⁴⁴⁸ Solids, **146**, 104196 (2021).
- ⁴⁴⁹ ⁴⁵F. Tisseur and K. Meerbergen, The quadratic eigenvalue problem, SIAM Review **43**, issue
⁴⁵⁰ 2 (2001), <https://doi.org/10.1137/S0036144500381988>.
- ⁴⁵¹ ⁴⁶Evgenii Narimanov, Ghost resonance in anisotropic materials: negative refractive index
⁴⁵² and evanescent field enhancement in lossless media, Adv. Photon. **1**, 046003 (2019).